Journal of the Ceramic Society of Japan 132 [12] 681-689 2024
DOI https://doi.org/10.2109/jcersj2.24090

JCS-Japan

FULL PAPER

Development of segmented titanium oxynitride layer with spinform surfaces exhibiting antibacterial properties

Masami Hashimoto[1,†], Norio Yamaguchi[1], Soma Hashimoto[1], Hidenobu Murata[1], Satoshi Kitaoka[1], Daisaku Yokoe[2], Taishi Ito[2], Takeharu Kato[2], Hiroyasu Kanetaka[3] and Hideki Kakisawa[4]

[1]Materials Research and Development Laboratory, Japan Fine Ceramics Center, 2–4–1 Mutsuno, Atsuta-ku, Nagoya 456–8587, Japan
[2]Nanostructures Research Laboratory, Japan Fine Ceramics Center, 2–4–1 Mutsuno, Atsuta-ku, Nagoya 456–8587, Japan
[3]Graduate School of Dentistry, Tohoku University, 4–1 Seiryo-machi, Aoba-ku, Sendai 980–8575, Japan
[4]National Institute for Materials Science, 1–2–1 Sengen, Tsukuba, Ibaraki 305–0047, Japan

We have developed the titanium oxynitride (TiON) layer which exhibits antibacterial activity against Escherichia coli without sunlight irradiation. This TiON layer with the segmented structure was formed on a pre-oxidized Ti substrate by the electron beam physical vapor deposition method while spraying the substrate and Ti target with N_2-0.1 % O_2 gas. An XRD pattern of the surface of the segmented layer revealed that the layer has a rock salt structure, which is preferentially deposited in a [111] direction to the substrate surface. TEM observation of the TiON layer showed that the columnar segments have a feather-like structure. The width of the segments near the surface was 100–500 nm, and their outermost surfaces were covered with nanometer-sized spines of 10–50 nm width. The TiON layer contained about 20 at % nitrogen as determined by XPS, and the surface was slightly negatively charged with a zeta potential of −0.9 mV at pH 7.2. The maximum average pressure in the elastic deformation region for the layer was over 100 MPa, which was much higher than the average occlusal pressure (<10 MPa). It is concluded that the segmental structure of the film facilitates the elastic deformation without distorting of the unique surface structure in response to external stress.

Key-words : Segmented TiON layer, Spinform, Electron beam physical vapor deposition, Antibacterial property, Nanoindentation

[Received August 8, 2024; Accepted September 26, 2024; Published online October 24, 2024]

1. Introduction

Ti and its alloys have extensive experience as a dental implant or an artificial hip joint because of its excellent corrosion resistance and biocompatibility due to the formation of a strong passive layer. Implant surfaces are required not only to bond to the alveolar bone, but also to have antibacterial properties, and other functions.

As a method to impart antibacterial properties to Ti and Ti alloys, immobilization of ions such as copper,[1] silver[2–5] or iodine[6,7] in the surface oxide layer is used to impart antibacterial properties to Ti implants, etc., and a controlled slow release of these ions, that is safe for living organisms is required. It has been reported that the antibacterial property is due to the release of these ions. When the antibacterial property is expressed by elution of ions, it is important to control the amount of immobilized ions and the elution rate.

There is also a method to immobilize a photocatalytically active film on Ti and Ti alloys to develop antibacterial properties. First, pure titanium is heat-treated in an ammonia atmosphere to form a nitrogen-incorporated titanium dioxide layer that exhibits antibacterial properties in response to visible light.[8] Second, TiON sputtered polyester surfaces are activated by sunlight irradiation, resulting in accelerated bacterial inactivation within minutes. The absorption in Kubelka–Munk units of the TiON film was observed to be directly proportional to the time of inactivation of Escherichia coli as determined by diffuse reflection spectroscopy.[9] These methods require exposure to light to develop antibacterial properties.

Recently, focusing on the fact that insect wings have a strong bactericidal effect, it was found that mimicking their surface shape can produce a very high bactericidal effect.[10–17] This function is expressed by transforming the surface of the component into a structure with a forest of spines of the order of several tens of nanometers in width, which rupture the cell membranes of bacteria attached to the surface of the spines. If the nanostructure can be simulated on the surface of an implant, it is expected to produce a revolutionary antibacterial property that is not dependent on drugs or other agents.

However, a load of approximately 100 kN is typically applied during tooth occlusion, and there is concern that such a ceramic layer with thin spines may be easily

† Corresponding author: M. Hashimoto; E-mail: masami@jfcc.or.jp

worn away by stress concentration caused by repeated occlusion.

Here, we focused on the electron beam physical vapor deposition (EB-PVD) technique, which enables coating with a unique surface structure.[18,19] For example, a target source of Y_2O_3 solid solution ZrO_2 (YSZ) is irradiated and the tip part is molten by an electron beam, and then a YSZ vapor deposited film is formed on a substrate placed at a predetermined position. The microstructure of the segments, such as the crystal orientation, void amounts, and spacings, and segment surface morphology, can be controlled by adjusting the deposition conditions, such as electron beam power, heating temperature and substrate rotation speed. This not only leads to the expectation that nanoscale spine surfaces will be formed, but also that the porous segments will exhibit deformation tolerance to external stress due to their low apparent Young's modulus. In other words, the destruction of the surface morphology, which has a spine structure with antibacterial properties, can be suppressed by relieving the stress concentration through local deformation of the contact area due to tooth occlusion.

We attempted to form a biocompatible TiO_2-based film with a spine structure on the surface of Ti, but considered a composition in which N was introduced to suppress diffusion and facilitate the formation of the spine structure.

In this study, we first explored the possibility of creating surface modified layers of TiON segments with spine surfaces of tens of nanometers on Ti substrates using EB-PVD, and then evaluated the antibacterial property without sunlight irradiation and the deformation tolerance of the segments to external stress.

2. Experimental procedure

2.1 Formation of TiON segmented layer by EB-PVD

A substrate for coating was prepared from high-purity Ti (Ti = 99.5 %, TI-452664, Nilaco Co., Tokyo, Japan), which is used as a model material for Ti implant alloys. After the substrate was cut to $\Phi 10 \times 3$ mm, the coating surface was polished to a mirror finish. In this study, to improve the adhesion between the Ti substrate and the TiON film, the mirror-polished substrate was pre-oxidized at 700 °C for 1 h in a N_2 atmosphere ($P_{O2} = 10^{-17}$ Pa) with P_{O2} adjusted by an oxygen pump according to the method described in Ref. 23) to form a rutile-type TiO_2 layer with a thickness of 70 nm on the substrate. This layer showed an exceptional ability to form apatite in artificial body fluids and to induce osteoblasts.

The pre-oxidized substrates were then mounted on a Ti jig in a chamber of an EB-PVD system with a semiconductor laser heating system. High-purity Ti (Ti = 99.5 %, $\Phi 40 \times 100$ mm, TI-452791, Nilaco Co., Tokyo, Japan) of the same grade as the substrates was used as the Ti target source. The distance between the target and the substrates was 600 mm. The substrates and the target were sprayed with N_2 gas containing a small amount of O_2 gas (N_2-0.1 % O_2) for sample A and O_2 gas for sample B at a flow rate of 100 cc/min. The fixture holding the substrates was rotated at 30 rpm during coating with a 12 kW electron beam power applied to the target. By rotating the substrate at this time, the deposition surface is periodically shadowed against the highly directional flow of the material vapor (shadowing effect), resulting in the formation of segments with a longitudinal crack structure in the thickness direction. The coating surfaces were heated to approximately 550 °C by laser irradiation and radiative heat transfer from the molten pool of the target. The total pressure in the chamber during coating was in the order of 0.1 Pa.

2.2 Surface structure analysis

The surface morphology of the samples was observed by scanning electron microscopy (SEM; SU8000, Hitachi High-Tech., Tokyo, Japan). The crystalline phases of the surface layers formed by the pre-oxidation and the subsequent coating were characterized by powder X-ray diffractometry with Bragg-Brentano geometry (SmartLab, Rigaku Corporation, Tokyo, Japan) with Cu Kα radiation at 40 kV and 50 mA. Incident slit was 1° and detector was D/tex Ultra 250. The surfaces were etched by Ar ion (4 kV) for 4 min at sputtering rate of 0.01 nm/min, and then the composition of the etched surface layers was evaluated by X-ray photoelectron spectroscopy (XPS; PHI X-tool, ULVAC-PHI, Kanagawa, Japan). The X-ray source was monochromatic Al Kα radiation at 14 kV and 25 mA. The binding energy was calibrated using the C 1s photoelectron peak of contamination carbon at 284.8 eV as a reference. XPS peak analysis was performed, Gauss-Shirley background was subtracted from all spectra before fitting.

2.3 Surface potential measurement

The zeta potential was measured under wet conditions, which corresponded to the electrostatic potential in the liquid medium. The Ti plates ($\Phi 10 \times 3$ mm) were prepared for zeta potential measurement as described in section 2.1. The pre-oxidized Ti and the surface coated by EB-PVD were electrically grounded to allow any stray charge to dissipate, and immediately placed in a zeta potential measurement apparatus (ELSZneo; Otsuka Electronics Co., Shiga, Japan) using a glass cell for the plate sample. The zeta potentials of three samples were measured in a 10 mM NaCl solution at pH 7.2.

2.4 Cross-sectional analysis of the segmented TiON layer

The Pt thin films on the outermost surfaces of the cross-sectional images were coated to prevent damage to the edges during cross-sectional processing with an ion milling device. The TiON layer formed on the pre-oxidized Ti substrate was thinned in a Hitachi NB5000 focused ion beam (FIB) scanning electron microscopy system at an accelerating voltage of 40–2 kV. Then, Ar ion beams with an accelerating voltage of 1–0.1 kV were then applied to the thinned specimen to remove the FIB-damaged layers on it using a Gatan PIPS II. Nanostructural character-

ization of the TiON layer was performed using a conventional transmission electron microscope (TEM) (JEM-F200, JEOL, Tokyo, Japan) equipped with dual EDS detectors having a total solid angle of 1.7 sr. Quantitative chemical composition maps of characteristic X-rays of Ti-Kα, N-Kα and O-Kα were obtained using the EDS system. Each pixel of these composition maps has the quantitative values of Ti-Kα, N-Kα and O-Kα, respectively. Ti/(N + O) and O/(N + O) value maps corresponding the compositional maps were drawn using Python (to study the distribution of N and O in the TiON).[20)]

2.5 Evaluation of antibacterial activity

As a preliminary test, a qualitative test for antibacterial susceptibility test was performed with $n = 2$. A nutrient agar was used in Petri dishes (Falcon® plastic dish for general bacteria, Corning Inc., New York, NY, USA) in 15 mL aliquots. Physiological saline was prepared by dissolving 8.5 g of sodium chloride (NaCl, Nacalai Tesque, Inc., Kyoto, Japan) in 1 L of ultrapure water, which was used after sterilization at 121 °C for 20 min in a high-pressure steam sterilizer. Escherichia coli (E. coli, JCM5491) was used as the test bacterial assay. It was used after being cultured on the nutrient agar medium at 37 °C for 24 h. The bacterial mass of the cultured E. coli was collected with a platinum loop and dispersed in physiological saline to prepare a stock bacterial suspension ($= 10^6$ CFU mL^{-1}). The bacterial suspension was seeded on each substrate (Ti, pre-oxidized Ti, sample A and sample B), followed by adhesion of the film and incubation at 37 °C for 24 h. After incubation, the samples were stained with acridine orange, a viable stain, and incubated at 37 °C for 1 h in the dark. After gentle rinsing with sterile PBS to remove excess staining agent, the live (green) bacteria on the substrates were examined under a fluorescence microscope (CKX53; Olympus, Tokyo, Japan).

2.6 Deformation property of films

Apparent Young's modulus, penetration depth, and average pressure were evaluated within an elastic deformation range during load application using the nano-indenter (TI 950 Triboindenter, Hysitron, MN, USA). The spherical indenter was used with a radius of 9.85 µm. The elastic deformation region satisfies Sneddon's expression (1),[21,22)] where P_m is the mean pressure, P is the applied load, R is the radius of the spherical indenter, h is the penetration depth of the indenter, and E is the apparent Young's modulus of the film.

$$P_m = \frac{P}{\pi R h} = \frac{4E}{3\pi}\left(\frac{h}{R}\right)^{0.5} \quad (1)$$

Since E remains constant in the elastic deformation, the region where $(3P)/(4R^{0.5}h^{1.5})$ remains constant as a function of h is assumed to be in the elastic deformation region. Therefore, the average value of the E and the corresponding P_m were determined at the maximum values of P and h in this region. The contact radius of indenter, r_c, is defined as $r_c = Rh^{0.5}$ for field swan approximation ($h_c = h/2$, where h_c is contact depth).

3. Results and discussion

3.1 Films formed by EB-PVD

Figure 1 shows the XRD patterns of the surfaces (a) before and (b) after the pre-oxidation of the Ti substrates, and the film surfaces of the samples (c) A and (d) B formed by the EB-PVD. Rutile-type TiO_2 was formed by the pre-oxidation of the substrates. For sample A as shown in Fig. 1(c), the diffraction peaks assigned to Ti phase becomes significantly smaller, and strong diffraction peaks identified to TiON with a rock salt structure (PDF#04-002-0430) were detected. This film is strongly oriented in the direction of the [111] plane. On the other hand, for sample B in Fig. 1(d), rutile-type TiO_2 phase with a very weak diffraction peak was detected instead of the peaks assigned to TiON.

Figure 2 shows the surface and cross-sectional SEM images of samples A and B. Sample A has segments about 2 µm thick with a vertical crack structure, and the width of each segment is several 100 nm, and the surface is composed of sharp edges. In contrast, sample B has a film with a thickness of about 1 µm was formed, and its surface was relatively smooth. In addition, the segment structure is not clear compared with that of sample A, and there are inhomogeneous vertical cracks in the direction of the film thickness at intervals of several micrometers, as shown by the arrows in the surface image.

Figures 3(a), 3(b), and 3(c) show the cross-sectional TEM image of sample A and the electron diffraction patterns of insets (i) and (ii) in the image, respectively. The near-surface carbon and W layers were coated to prevent edge damage during the cross-sectional milling of the sample. Both (i) and (ii) in the insets refer to TiON. The TiON segments show a feather-like structure with a pyramidal tip and their surfaces covered with nano-spines.

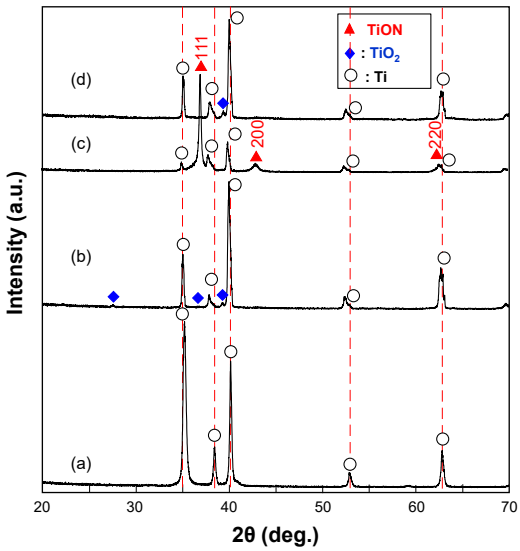

Fig. 1. X-ray diffraction patterns of the surfaces of (a) before and (b) after the pre-oxidation of the Ti substrates, and the film surfaces of the samples (c) A and (d) B formed by the EB-PVD.

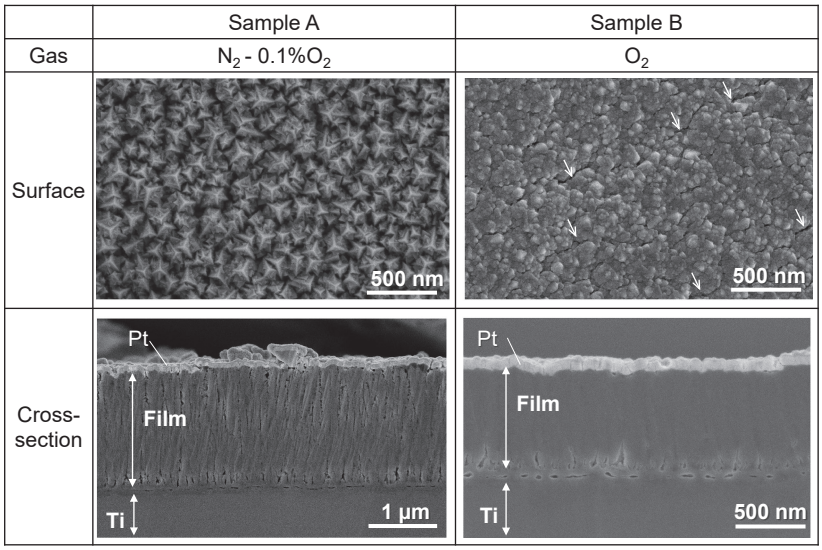

Fig. 2. SEM photographs of the surface and cross-section of the samples A and B.

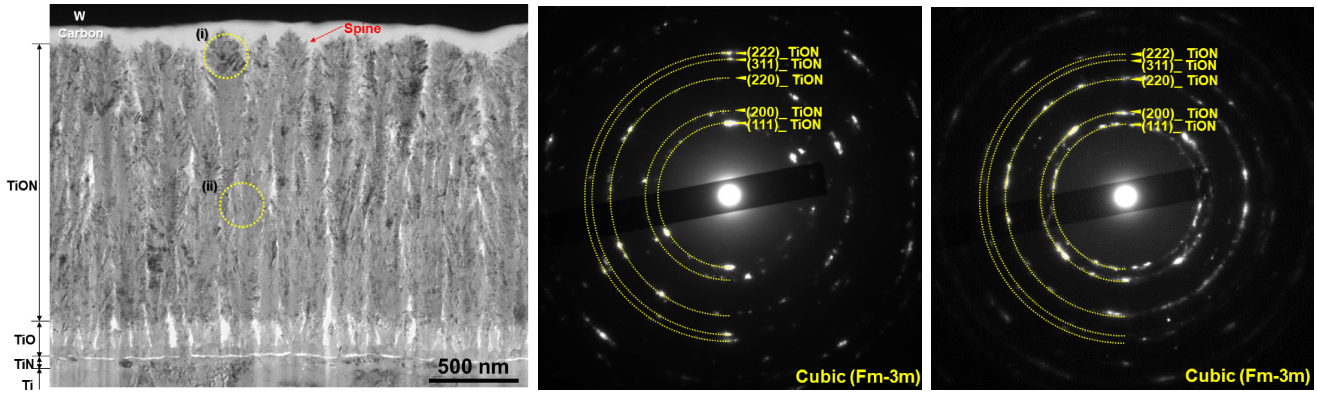

(a) (b) (c)

Fig. 3. Cross-sectional TEM image of the sample A (a). (b) and (c) are the electron diffraction patterns collected from the region marked with a white circle in the TEM image (i) and (ii), respectively. Insets (i) and (ii) show the TiON.

The widths of the segments increase toward the surface. The widths of the top of the segments measured in the image in Fig. 3(a) are between 100 and 500 nm, and those of the spines are between 10 and 50 nm. The film consists of a TiN layer, a TiO layer, and a TiON layer in order from the side of the Ti substrate. The TiN layer progresses due to the nitridation reaction at the Ti–TiO_2 scale interface when the Ti substrate is pre-oxidized in an N_2 environment under low P_{O2} conditions at 973 K. It is thermodynamically formed with a P_{O2} of 10^{-23} Pa or lower.[23)]

When a film is deposited by the EB-PVD method, the surface temperature of the film to be deposited is generally exposed to high temperatures of 500 °C or higher due to the radiant heat associated with the melting of the surface of the target source by electron beam irradiation. The concern here is that the spines on the surface may disappear due to accelerated surface diffusion on the film during high-temperature deposition, resulting in a smooth surface. But covalent bonding characteristics in a Ti–O film, which is expected to have biocompatibility, can be strengthened by N-doping in the film, resulting in the formation of the spine surface.

Figure 4 shows the high-resolution TEM image of the tip of the segment of sample A. The lattice spacing of the TiON layer is 0.245 nm, which corresponds to the lattice spacing of the (111) plane of TiON (ICSD426340) with rock salt structure. The TiON crystal is oriented in a direction of the [111] plane relative to the substrate, which is consistent with the XRD pattern of Fig. 1(c). The surface energy of TiON is highest in the (111) plane, followed by the (110) and (100) planes, in that order. The (111) plane is unstable because it is composed of the same type of atoms and the surface is highly charged. The (100) layer is the most stable layer because the Ti, N, and O atoms alternate like a checkerboard, and their positive and negative charges cancel each other out. The (110) plane, with alternating rows of Ti atoms and rows of O and N atoms, is electrically neutral but not as stable as the (100) plane. The TiON layer produced by EB-PVD grows preferentially towards the (111) plane, which has a high surface energy,

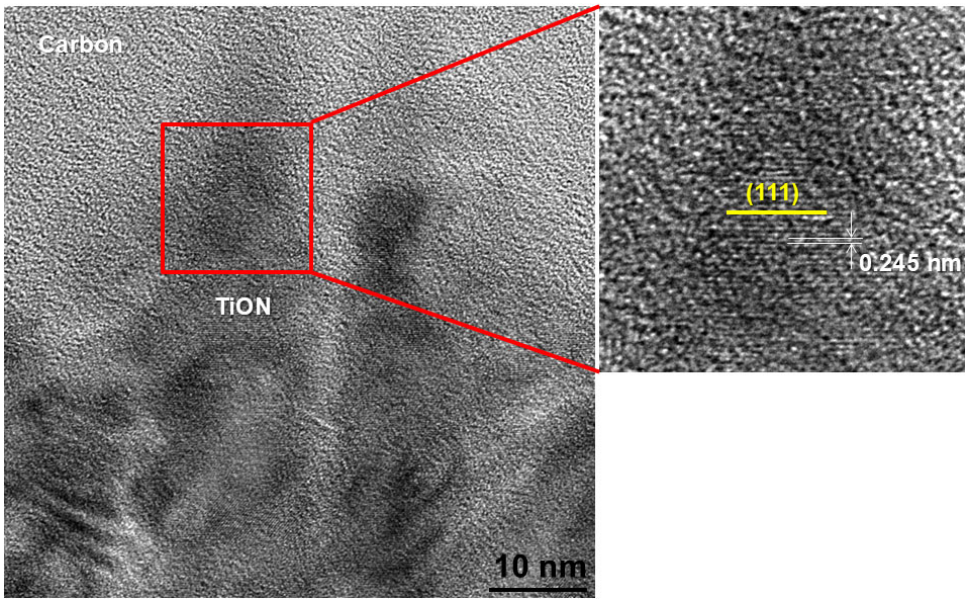

Fig. 4. High-resolution TEM image of the tip of the segment of sample A.

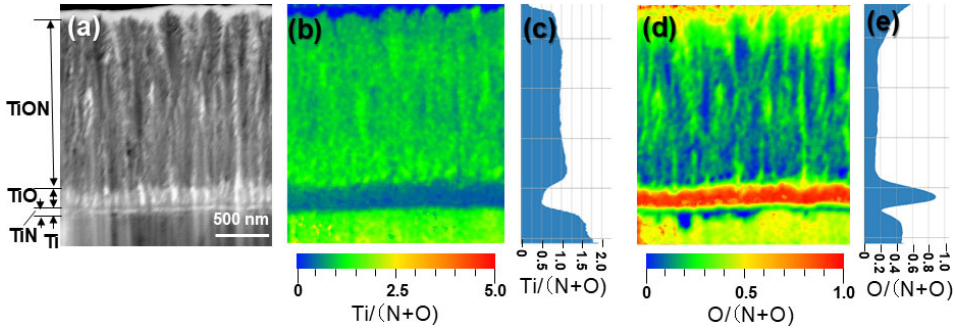

Fig. 5. Bright-field STEM image and the corresponding elemental ratio maps using EDS elemental distribution data of the cross-section of the sample A; (a) STEM image, (b) Ti/(N + O), (c) vertical average of Ti/(N + O) ratio, (d) O/(N + O) and (e) vertical average of O/(N + O) ratio.

and also forms the (100) and (110) planes, which have a low surface energy, and are thought to form a sharp-tipped surface.

Figure 5 shows the bright field STEM image and the corresponding elemental ratio maps using the EDS elemental distribution data of the cross section of sample A; (a) STEM image, (b) Ti/(N + O), (c) vertical average of Ti/(N + O) ratio, (d) O/(N + O) and (e) vertical average of O/(N + O) ratio. The film consists of a TiN layer, a TiO layer, and a TiON layer in order from the side of the Ti substrate. As shown in Figs. 5(b) and 5(d), the surface of the TiON segments is oxygen rich compared to the interior, and the interface between the segments and the substrate is nitrogen rich. In addition, the Ti/(N + O) ratio near the surfaces of the segments is about 0.8, which is oxygen-rich compared to 1.0 for the insides. When a Ti substrate was preoxidized at 700 °C in N_2 gas with an extremely low O_2 concentration controlled by an oxygen pump, a layer with a rutile structure with a only 70 nm thick was formed on the substrate as shown in Fig. 1(b), and a TiN layer was also formed just below the scale.[23] Therefore, the nitrogen-rich layer just above the substrate in Fig. 5 is considered a TiN layer. However, the thickness of the O-rich layer in Fig. 5 is sufficiently greater than that of the rutile scale formed by the pre-oxidation. The oxygen-rich segments are probably formed, because the oxygen partial pressure became locally high near the coating surface due to the reduction of the oxide in the initial stage of the segment deposition at 550 °C.

The surfaces of samples A and B were each analyzed by XPS, and the compositions were analyzed based on the binding energy values obtained from the photoelectron spectra. **Figures 6**(a) and 6(b) show the Ti_{2p} and N_{1s} XPS spectra of samples A and B, respectively. Only sample A contained nitrogen, and the composition of the layer was $Ti_{45.2}O_{31.8}N_{23.0}$. Ti/(O + N) is 0.82, which means that the surface of sample A was Ti poor structure, which is consistent with the EDS result as shown in Fig. 5(c).

In the case of $Ti_{2p3/2}$ level of sample A, the binding energy of TiN, TiON and TiO_2 were determined to be 454.5, 456.3 and 458.3 eV, respectively.[9] The fractions of TiN, TiON and TiO_2 determined from the deconvoluted

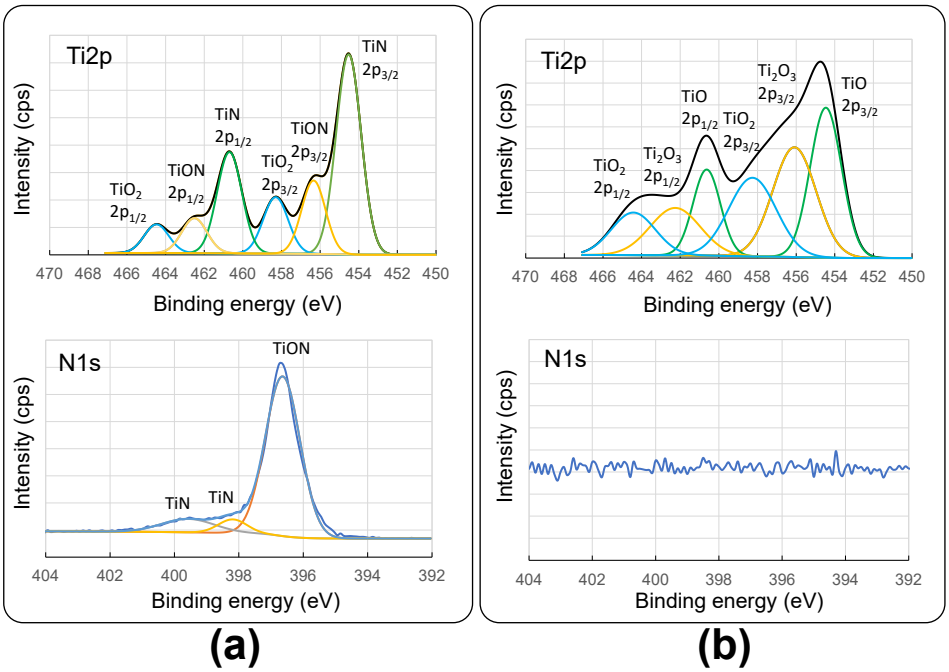

Fig. 6. Ti_{2p} and N_{1s} XPS spectra of the surfaces of samples (a) A and (b) B.

spectrum were 40.8, 14.3 and 11.5 area %, respectively. The presence of N in the sample A was characterized by using XPS, the major Ti–N bond in TiON and the minor chemisorbed N–O bond in N_{1s} core levels were located at 397.4 and 401.7 eV, respectively as shown in Fig. 6(a). Therefore, the oxygen was incorporated into the rock salt TiN structure during the deposition process under N_2-0.1 %O_2 gas flow. Furthermore, it suggests the presence of trace amounts of TiO_2 near the surfaces of the segments. On the other hand, the composition of the layer of sample B was $Ti_{33.7}O_{66.3}$. In the case of $Ti_{2p3/2}$ layer of sample B, the binding energy of TiO, Ti_2O_3 and TiO_2 were located at 454.5, 456.1 and 458.3 eV, respectively.[24] The fractions of TiO, Ti_2O_3 and TiO_2 determined from the deconvoluted spectrum were 35.7, 36.0 and 28.3 area %, respectively.

The average zeta potentials at pH 7.2 for samples A and B were -3.7 ± 1.1 mV and -23.5 ± 0.4 mV, respectively. The fact that the zeta potential of sample B was more negative than that of sample A suggests that the surface of sample B is covered with a greater number of negatively charged oxygen ions.

3.2 Antibacterial property

After 24 h of the incubation, fluorescence microscopy images showed that (a) the Ti substrate, (b) the pre-oxidized substrate, and (d) the sample B are covered with numerous and scattered viable bacteria as shown in **Fig. 7**. In contrast, a few live bacteria were observed on sample A as shown in Fig. 7(c). As for the reason why sample A developed antibacterial properties, firstly, the zeta potential of the segmented TiON membrane is slightly negatively charged (-0.94 ± 1.62 eV), which is believed to cause an electrical repulsion between it and the negatively charged bacteria. However, the zeta potential of pre-oxidized Ti and sample B were -6.6 ± 0.25 and -6.45 ± 1.36 eV, respectively. On sample A, it is unlikely that bacteria adhesion is reduced due to electrostatic repulsion between the substrate and bacteria. Possible denaturation mechanisms of bacterial proteins related to antimicrobials include oxidation by the Mars-van-Krevelen mechanism,[25,26] S–S bond cleavage,[27] acid-base reactions,[28] and hydrogen bond cleavage.[29] The TiON film does not contain Mg, Fe or Cu elements that affect protein denaturation. There are reports that the number of bacteria on TiON[9] and TiN[30] with a smooth surface is reduced by about 50 to 60 % even in the dark. However, as shown in Fig. 7(c), almost no live bacteria are observed on spiny TiON, so there may be a cause for the antibacterial properties that does not appear on smooth surfaces. Therefore, another factor may be involved in the antibacterial susceptibility.

The TiON layer consists of 100–500 nm segments with 10–50 nm spines on the surface [Fig. 3(a)]. Segmental structured surfaces produced by the EB-PVD process have spikes on the surface that are equivalent in size to those effective for antibacterial properties. In order to kill bacteria that come in contact with the surface, research is underway to control the surface topography (physical geometry, nanostructure, nanotexture) of Ti.[31–34] The nanostructured surfaces have earned their reputation as mechanobactericidal surfaces, independent of chemical effects, because the functionality (ability to kill bacteria) has been shown to persist across different materials. Thus, we believe that when bacteria adhere to the spicule, their cell membranes are destroyed and killed, thus inhibiting bacterial growth and causing the development of antibacterial properties.

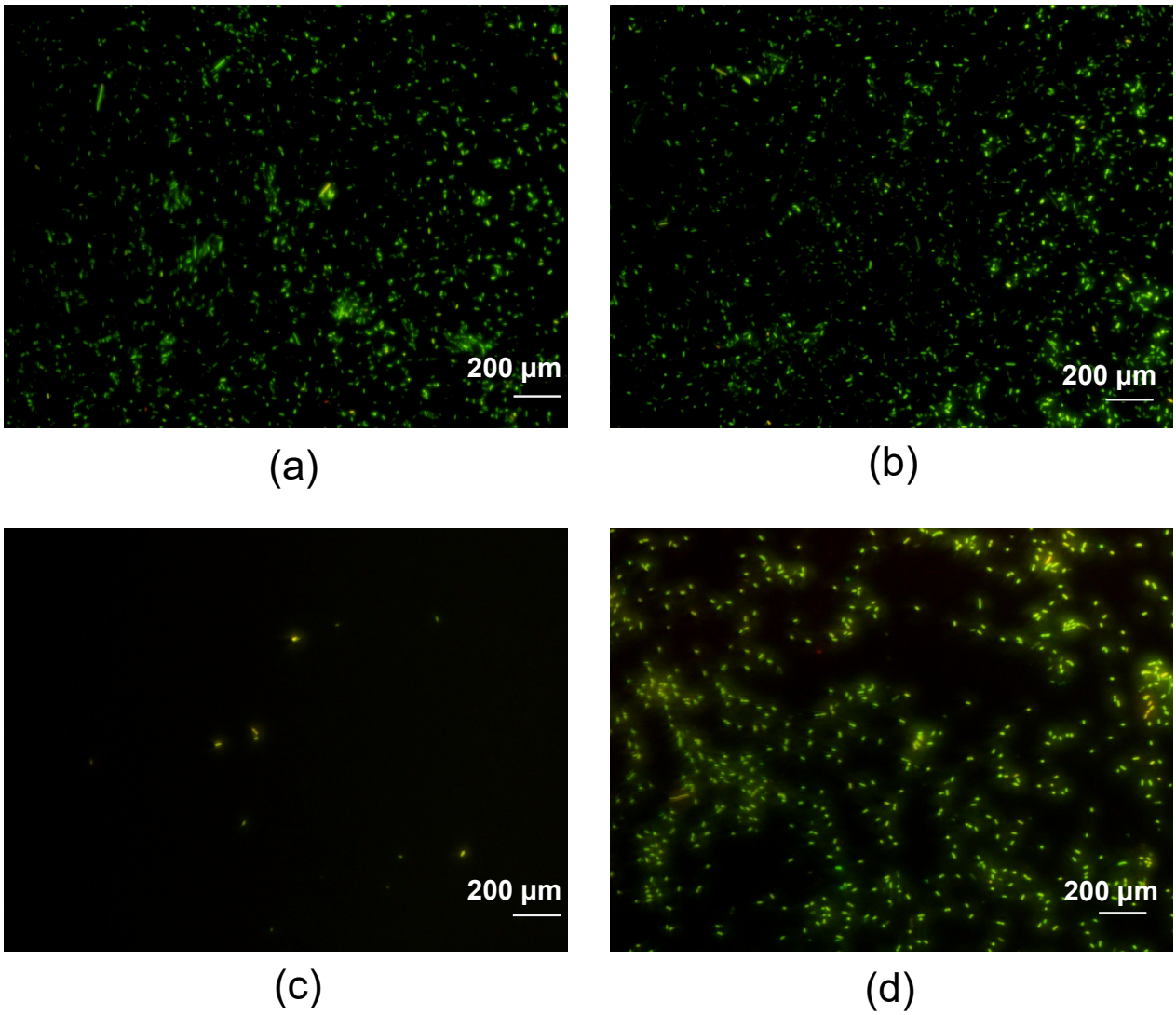

Fig. 7. Viable bacteria stained with live assay on (a) before, (b) after the pre-oxidation of the Ti substrates, (c) sample A and (d) sample B ($n = 2$).

3.3 Deformation property of films

The nano-spiked segments were found to have antibacterial properties. In order to understand the deformation tolerance of the segment under occlusal conditions, the deformation characteristics of the elastic deformation region were investigated using the nanoindentation technique with the spherical indenter. **Figure 8**(a) shows the typical indentation load P versus penetration depth h curves for samples A and B. The maximum applied load (P_{max}) was set to 1,000 μN. The maximum penetration depth (h_{max}) at the P_{max} for sample A is greater than that for sample B. The reproducibility of the p-h curve for sample A is good, but for sample B it varies widely. This is presumed to be because the through cracks exist unevenly in the film thickness direction of sample B. Assuming that Sneddon's equation[21,22] is satisfied within the elastic deformation range of the films, the apparent Young's modulus (E) for elastic deformation and the maximum deformation depth ($h_{e\text{-}max}$) within the deformation range are obtained. Figure 8(b) shows the relationship between $(3P)/(4R^{0.5}h^{1.5})$ and h for each curve in Fig. 8(a). The E and $h_{e\text{-}max}$ (arrows in the figure) for each curve are determined from the region where a value on the longitudinal axis in Fig. 8(b) is constant. The length of the flat area in Fig. 8(b), sample A has a longer elastic deformation range.

Figure 9 shows (a) E, (b) $h_{e\text{-}max}$, and (c) average pressure at $h_{e\text{-}max}$ within the elastic deformation region of samples A and B. Each value is the average of three data. The E value of sample A is 1/4 of that of sample B, and the $h_{e\text{-}max}$ of sample A is larger than that of sample B. Since the average maximum indentation depth $h_{e\text{-}max}$ of the indenter in the elastic deformation region of sample A is 23 nm, the indenter contact radius r_c is 475 nm and the indenter contact area S is 0.708 μm^2. Assuming that the segment width (diameter) is 150 nm, the number of segments in the above contact area above is 40. On the other hand, since the average $h_{e\text{-}max}$ of sample B is 12 nm, the r_c is 343 nm and the S is 0.369 μm^2. As previously mentioned, the variability in the load-depth curves of sample A was smaller than that of sample B, and the apparent

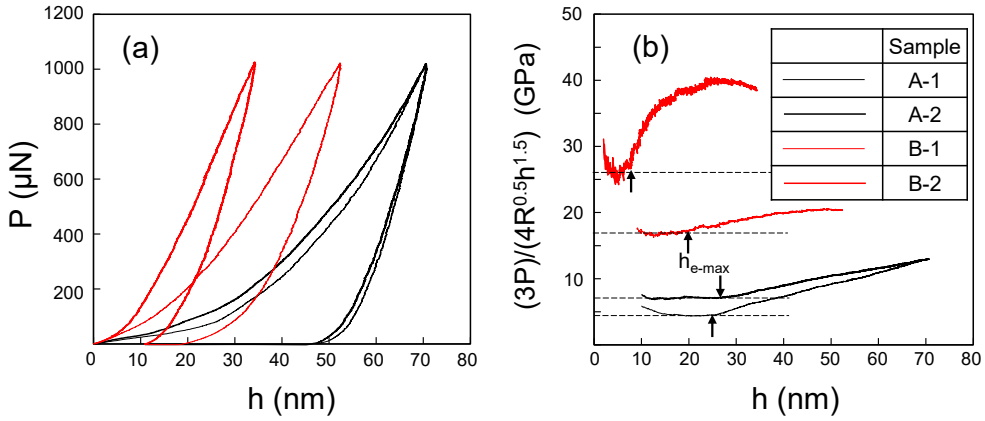

Fig. 8. Typical indentation load P versus penetration depth h curves for samples A and B (a). (b) shows relationship between $(3P)/(4R^{0.5}h^{1.5})$ and h for each curve of (a).

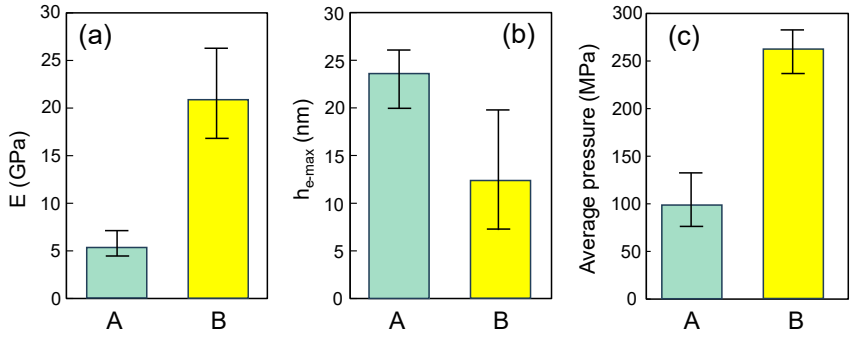

Fig. 9. Apparent Young's modulus (a), indentation depth at max. load (b) and average pressure at max. load within the elastic deformation region (c) of samples A and B.

Young's modulus of the sample A was lower with a longer elastic deformation range. In the case of sample A, each segment deforms slightly in response to the indentation by the indenter, which reduces the stress concentration at the indenter contact area, allowing the entire film to undergo significant deformation. On the other hand, in sample B, where the segments were thicker and less deformable, the stress is more likely to be concentrated at the indenter contact area, making it more susceptible to the influence of the segment shape at that area.

4. Conclusions

The electron beam PVD method deposited TiON layer oriented in the [111] direction on the pre-oxidized Ti substrate by heating at 550 °C while blowing N_2-0.1 %O_2. The N content in the TiON layer was about 20 at %, and the width of the top surface of the columnar segments constituting the layer was 100 to 500 nm. The width of the spines ranged from 10 to 50 nm. The TiON layers showed antibacterial activity against E. coli. This may be mainly due to the disruption of the cell membrane by the spiky structure. The TiON layer is easily deformed by external stress. The average pressure at maximum load in the elastic deformation zone of the layer is much higher than the average occlusion pressure. In the future, it will be necessary to develop TiON films that are not only antibacterial, but also biocompatible.

Acknowledgments This research was supported by JSPS Grant-in-Aid for Scientific Research 21H01644 and 19H05792. We would like to thank Drs. Hideyuki Murakami and Kimiyoshi Naito, NIMS, and Dr. Takashi Akatsu, Tokyo University of Technology, for their cooperation and useful advice on the measurement and analysis methods of nano-indentation.

References

1) K. Suzuki, T. Yokoi, M. Iwatsu, M. Furuya, K. Yokota, T. Mokudai, H. Kanetaka and M. Kawashita, *J. Asian Ceram. Soc.*, 9, 1448–1456 (2021).
2) K. Suzuki, M. Iwatsu, T. Mokudai, M. Furuya, K. Yokota, H. Kanetaka, M. Shimabukuro, T. Yokoi and M. Kawashita, *Molecules*, 28, 650 (2023).
3) A. Skovager, K. Whitehead, D. Wickens, J. Verran, H. Ingmer and N. Arneborg, *Colloid. Surface. B*, 109, 190–196 (2013).
4) Y. Okuzu, S. Fujibayashi, S. Yamaguchi, K. Masamoto, B. Otsuki, K. Goto, T. Kawai, T. Shimizu, K. Morizane, T. Kawata, Y. Shimizu, M. Hayashi and S. Matsuda, *J. Biomater. Appl.*, 35, 670–680 (2021).
5) K. Masamoto, S. Fujibayashi, S. Yamaguchi, B. Otsuki, Y. Okuzu, T. Kawata, K. Goto, T. Shimizu, Y. Shimizu, T. Kawai, M. Hayashi, K. Morizane, M. Imamura, N. Ikeda, Y. Takaoka and S. Matsuda, *J. Biomed. Mater. Res. B*, 109, 238–245 (2020).
6) N. Ikeda, S. Fujibayashi, S. Yamaguchi, K. Goto, B. Otsuki, T. Kawai, T. Shimizu, Y. Okuzu, K. Masamoto,

Y. Shimizu, Y. Takaoka and S. Matsuda, *Biomat. Adv.*, 138, 212952 (2022).
7) S. Yamaguchi, P. T. M. Le, S. A. Shintani, H. Takadama, M. Ito, S. Ferraris and S. Spriano, *Nanomaterials-Basel*, 11, 2199 (2021).
8) M. Kawashita, N. Matsui, T. Miyazaki and H. Kanetaka, *Colloid. Surface. B*, 111, 503–508 (2013).
9) S. Rtimi, C. Pulgarin, M. Bensimon and J. Kiwi, *Sol. Energy*, 93, 55–62 (2013).
10) S. Hawi, S. Goel, V. Kumar, O. Pearce, W. N. Ayre and E. P. Ivanova, *ACS Appl. Nano Mater.*, 5, 1–17 (2022).
11) K. A. Whitehead, D. Rogers, J. Colligon, C. Wright and J. Verran, *Colloid. Surface. B*, 51, 44–53 (2006).
12) N. Ogawa, K. Sato, K. Sunada, H. Ishiguro, H. Kojima and T. Ito, *J. Photopolym. Sci. Tec.*, 35, 213–217 (2022).
13) L. Ploux, K. Anselme, A. Dirani, A. Ponche, O. Soppera and V. Roucoules, *Langmuir*, 25, 8161–8169 (2009).
14) E. Fadeeva, V. K. Truong, M. Stiesch, B. N. Chichkov, R. J. Crawford, J. Wang and E. P. Ivanova, *Langmuir*, 27, 3012–3019 (2011).
15) Y. Inoue, M. Uota, T. Torikai, T. Watari, I. Noda, T. Hotokebuchi and M. Yada, *J. Biomed. Mater. Res. A*, 92, 1171–1180 (2009).
16) S. Ferraris, A. Venturello, M. Miola, A. Cochis, L. Rimondini and S. Spriano, *Appl. Surf. Sci.*, 311, 279–291 (2014).
17) E. P. Ivanova, J. Hasan, H. K. Webb, G. Gervinskas, S. Juodkazis, V. K. Truong, A. H. F. Wu, R. N. Lamb, V. A. Baulin, G. S. Watson, J. A. Watson, D. E. Mainwaring and R. I. J. Crawford, *Nat. Commun.*, 4, 1–7 (2013).
18) N. Yamaguchi, K. Wada, K. Kimura and H. Matsubara, *J. Ceram. Soc. Jpn.*, 111, 883–889 (2003).
19) T. Yokoi, N. Yamaguchi, M. Tanaka, D. Yokoe, T. Kato, S. Kitaoka and M. Takata, *Mater. Lett.*, 193, 176–178 (2017).
20) S. Kitaoka, M. Tanaka, N. Kawashima, T. Ito, D. Yokoe, T. Kato, T. Ogawa, N. Yamazaki, N. Hosoya and T. Nakamura, *J. Am. Ceram. Soc.*, 106, 4863–4876 (2023).
21) T. Akatsu, S. Numata, T. Demura, Y. Shinoda and F. Wakai, *Mech. Mater.*, 83, 66–71 (2015).
22) T. Akatsu, S. Numata, T. Demura, Y. Shinoda and F. Wakai, *Mech. Mater.*, 92, 1–7 (2016).
23) M. Hashimoto, T. Ogawa, S. Kitaoka, S. Muto, M. Furuya, H. Kanetaka, M. Abe and H. Yamashita, *Acta Mater.*, 155, 379–385 (2018).
24) NIST X-ray Photoelectron Spectroscopy Database (SRD 20) Ver. 5.0.
25) R. Kiribayashi, K. Sunada, Y. Mochizuki, T. Isobe, S. Matsushita, T. Nagai, H. Ishiguro and A. Nakajima, *J. Ceram. Soc. Jpn.*, 131, 117–125 (2023).
26) R. Nakane, R. Kiribayashi, K. Sunada, Y. Mochizuki, T. Isobe, S. Matsushita, T. Nagai, H. Ishiguro and A. Nakajima, *Ceram. Int.*, 50, 10797–10805 (2024).
27) M. Minoshima, Y. Lu, T. Kimura, R. Nakano, H. Ishiguro, Y. Kubota, K. Hashimoto and K. Sunada, *J. Hazard. Mater.*, 312, 1–7 (2016).
28) N. Aničić, M. Vukomanović, T. Koklič and D. Suvorov, *Small*, 14, 1800205 (2018).
29) S. Legmairi, S. Meneceur, G. G. Hasan, L. S. Eddine, H. A. Mohammed, F. Alharthi and J. A. A. Abdullah, *Nanotechnology*, 34, 445101 (2023).
30) Y. Bao, W. Wang, W. Cui and G. Qin, *Surf. Coat. Tech.*, 419, 127296 (2021).
31) E. Fadeeva, V. K. Truong, M. Stiesch, B. N. Chichkov, R. J. Crawford, J. Wang and E. P. Ivanova, *Langmuir*, 27, 3012–3019 (2011).
32) A. Jemat, M. J. Ghazali, M. Razali and Y. Otsuka, *BioMed Res. Int.*, 2015, 791725 (2015).
33) F. H. Rajab, C. M. Liauw, P. S. Benson, L. Li and K. A. Whitehead, *Colloid. Surface. B*, 160, 688–696 (2017).
34) S. Spriano, S. Yamaguchi, F. Baino and S. Ferraris, *Acta Biomater.*, 79, 1–22 (2018).